

A 77-GHz FMCW MIMO Radar Based on an SiGe Single-Chip Transceiver

Reinhard Feger, *Student Member, IEEE*, Christoph Wagner, *Student Member, IEEE*, Stefan Schuster, *Member, IEEE*, Stefan Scheiblhofer, *Member, IEEE*, Herbert Jäger, *Member, IEEE*, and Andreas Stelzer, *Member, IEEE*

Abstract—This paper describes a novel frequency-modulated continuous-wave radar concept, where methods like nonuniform sparse antenna arrays and multiple-input multiple-output techniques are used to improve the angular resolution of the proposed system. To demonstrate the practical feasibility using standard production techniques, a prototype sensor using a novel four-channel single-chip radar transceiver in combination with differential patch antenna arrays was realized on off-the-shelf RF substrate. Furthermore, to demonstrate its practical applicability, the assembled system was tested in real world measurement scenarios in conjunction with the presented efficient signal processing algorithms.

Index Terms—Array processing, FM radar, radar.

I. INTRODUCTION

THE USE of radar systems for civil applications has increased significantly over the last years. The development of complete integrated radar circuits operating in the millimeter-wave range has led to a low-cost and compact realization of multichannel systems [1], [2].

Such systems can not only be used for the classical target range and velocity measurement, but add the capability to measure the angular position of targets relative to the radar. Contrary to the range and velocity measurement problem, where resolution of different targets is coupled to the used bandwidth and measurement time, the angular resolution is determined by the aperture of the used antenna array. This leads to one of the major challenges in array processing: to improve the angular resolution, it is necessary that the antenna array's aperture is increased, but in order to avoid the violation of the sampling theorem in the spatial domain, it is inevitable to keep the distances between the array elements smaller than $\lambda/2$, where λ denotes the free-space wavelength at the highest used frequency, which, in turn, leads to a large number of necessary array elements and therefore channels. This is often not feasible because of the resulting high hardware complexity and the large amount of data that is generated from the increased number of channels.

Manuscript received September 29, 2008; revised January 30, 2009. First published April 14, 2009; current version published May 06, 2009.

R. Feger, C. Wagner, S. Schuster, S. Scheiblhofer, and A. Stelzer are with the Christian Doppler Laboratory for Integrated Radarsensors, Institute for Communications and Information Engineering, Johannes Kepler University, 4040 Linz, Austria (e-mail: r.feger@icie.jku.at).

H. Jäger is with Danube Integrated Circuits Engineering (DICE) GmbH, 4040 Linz, Austria (e-mail: herbert.jaeger@infineon.com).

Color versions of one or more of the figures in this paper are available online at <http://ieeexplore.ieee.org>.

Digital Object Identifier 10.1109/TMTT.2009.2017254

To reduce the number of channels that have to be processed simultaneously, the use of switched arrays has been proposed [3]. Additionally, numerous researchers investigate the use of advanced signal processing algorithms to increase the angular resolution without increasing the array's aperture. For an overview on this topic, see, for example, [4] and the references therein. These methods allow the inclusion of additional knowledge into the signal processing part of the radar (e.g., the number of existing targets, their rough angular position, incoherence of signals from different targets, etc.), but many of these algorithms achieve their superior performance only if the assumptions on the prior information are fulfilled exactly, otherwise they perform very poorly. Often the performance is even worse than that obtained with the more robust classical estimation algorithms, which do not consider the additional information in this situation. For example, the very popular MUSIC [5] and ESPRIT [6] algorithms rely on the fact that signals arriving from different targets are incoherent and the number of targets is known. As will be shown, the incoherence assumption does not hold for frequency-modulated continuous-wave (FMCW) systems with multiple static targets positioned in the same range relative to the radar, which makes it impossible to detect and distinguish these targets in such a scenario. Although methods that allow the application of these algorithms in the coherent signals case have been developed [7], [8] and their applicability to real world measurement data has been shown [9], the practical use is limited because of the need to know the exact number of existing targets. This information is seldom available in practice, and therefore, has to be estimated via additional signal processing steps to determine the model order, e.g., using criteria discussed in [10] and [11]. Apart from the additional processing, and therefore, system complexity that the use of these algorithms implicates, they are only usable at high or moderate signal-to-noise ratios (SNRs).

In this paper, we therefore propose a combination of different hardware based methods to increase the angular resolution while keeping the number of channels small. The signal processing is based on a conventional delay-and-sum beamformer [4], which is known to be robust against modeling uncertainties and can be used as an estimator for the number of signals as well. To allow for a compact sensor design, the use of a single-chip solution is preferable, but due to the limited chip size and number of available pads, a high number of RF channels is prohibitive. We overcome this problem via the application of the multiple-input multiple-output (MIMO) technique, which is used to synthesize virtual antennas [12]. In the presented case, the MIMO principle allows to synthesize ten dif-

ferent array element positions from only four physical existing RF channels. To further increase the angular resolution, we utilize a sparse antenna array. This technique allows to increase the distance between the array elements without causing ambiguities due to the spatial undersampling [13]. The combination of these two methods allows array element spacings larger than $\lambda/2$ for physically neighboring antenna pairs without causing ambiguities near endfire. Hence, mutual coupling effects between the array elements, which possibly degrade the system's performance [14], [15], are substantially reduced. Additionally the single array elements can be bigger, which makes a tradeoff between antenna gain and the achievable field of view (FOV) possible. To realize a MIMO radar system, a silicon-germanium (SiGe)-based four-channel transceiver (TRX) has been developed that allows a reconfiguration of its cells on the fly to operate as receiver (RX) or as TRX.

This paper is organized as follows. First, the TRX and its reconfigurable cells are described. Based upon this, Section III presents the used signal model, which shows how to synthesize virtual antennas using the MIMO principle. In Section IV, a possible signal processing approach based on the delay-and-sum beamformer and a method for array calibration is presented. The results from this section are then used for the design of the sparse antenna array using a convex optimization approach. Section VI gives a short description of the frontend and the baseband hardware, which is used for generating measurement data. Finally, Section VII presents different measurement results from multiple scenarios collected in an anechoic chamber and outdoors.

II. SiGe BASED FOUR CHANNEL TRX

A. TRX Cells

As already mentioned, the aim of this study is the development of an FMCW radar sensor using a single-chip TRX consisting of four TRX cells. To allow the synthesis of virtual antenna elements, the realized cells should be reconfigurable on the fly to work either in RX or TRX mode, as will be shown later. This is achieved utilizing a ratrace coupler and two amplifiers, as shown in Fig. 1. A similar structure was also used in [16]. The function is as follows. In the TRX mode, the switchable amplifier 1 (AMP1) is activated and the cell operates comparable to a standard single antenna radar. The output signal from AMP1 is splitted, one-half is terminated in the termination, while the other half is fed to the antenna port. The RX mixer's RF port is isolated from the transmit (TX) amplifier. On the other hand, the RX signal is also split up and half of the power is fed into the RX mixer's RF port, while the other half is terminated at the output of AMP1. To activate the RX-only mode, AMP1 is deactivated, and therefore, no TX signal is sent to the antenna. Since amplifier 2 (AMP2) has two outputs, the RX mixer is still provided with local oscillator (LO) power in this mode, and therefore, the RX part is not influenced by the state of AMP1.

B. Four-Channel TRX Chip

The central building block of the presented radar system is the fully differential four channel TRX chip, as shown in Figs. 2 and 3, which allows the implementation of a MIMO radar due to its reconfigurable cells. It consists of four TRX cells, as presented

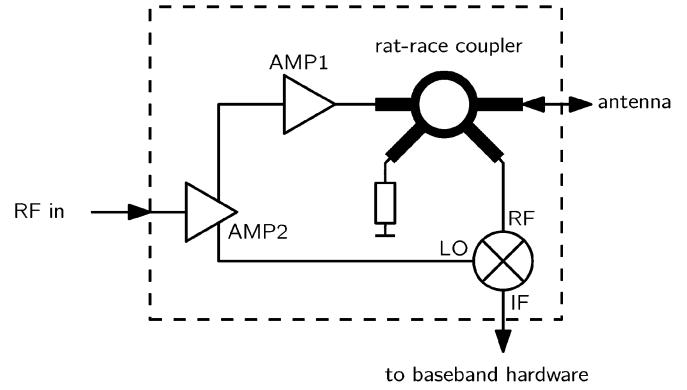


Fig. 1. Schematic of the reconfigurable TRX cell used to realize the four channel TRX chip.

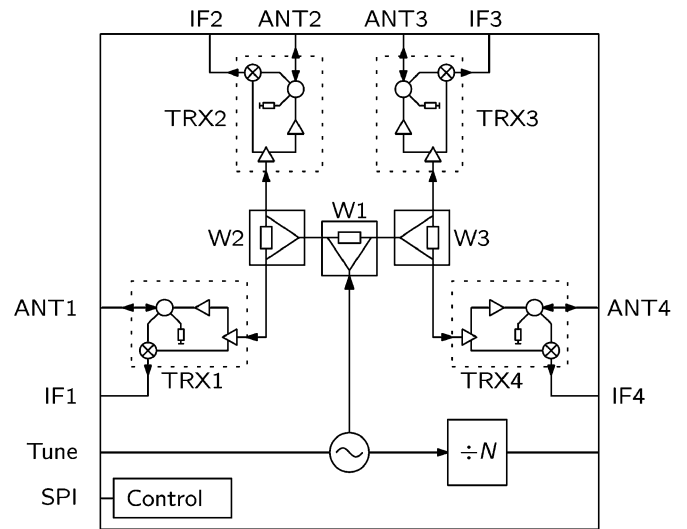


Fig. 2. Block diagram showing the configuration of the complete four-channel TRX chip.

in Section II-A, a voltage-controlled oscillator (VCO) to generate the RF power at 77 GHz, Wilkinson dividers (W1–W3) to distribute the RF power, and a frequency divider providing a lower frequency RF signal derived from the VCO output. The implemented control logic allows the reconfiguration of the chip via a synchronous serial interface. All RF and IF ports are realized as differential interfaces. An output power of 2 dBm at each channel was measured on board, which means that losses occurring due to the bond-wire transition are already included. In the RX mode, an isolation better than 20 dB between the input and the antenna port of a TRX cell is achieved. Fig. 3 shows a micrograph of the SiGe chip.

III. MIMO SIGNAL MODEL AND SYNTHESIS OF VIRTUAL ANTENNAS

A. MIMO Radar Fundamentals

MIMO radar is an emerging technology that is an extension to the classical digital beamforming radar. The main difference compared to a conventional radar is the capability of transmitting different signals on multiple TX antennas while keeping these signals separable at reception. This separation capability

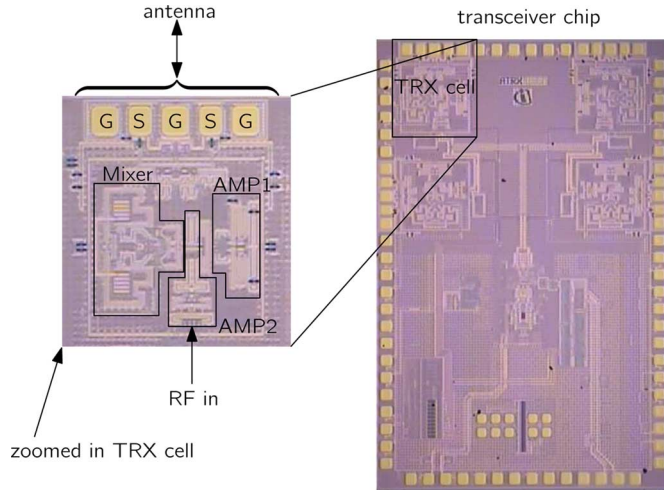


Fig. 3. Micrograph of the fully differential SiGe TRX chip fabricated by Infineon Technologies AG, with labels highlighting the most important building blocks. A detailed description of the TRX cell can be found in [16].

is the major characteristic shared between all MIMO radar systems and leads to various advantages that have been investigated by numerous researchers. One advantage of using multiple TXs is that the target is illuminated from different directions. Therefore, the negative effects of a strongly angle-dependent target radar cross section (RCS) can be reduced [17]. To achieve a considerable benefit from this fact, the TXs need to be widely separated, which conflicts with our aim of developing a compact sensor. However, the MIMO principle offers more advantages. In [12], it was shown that it is possible to synthesize virtual antenna positions leading to a larger number of effective array elements. Therefore, the number of resolvable targets in the same range bin is increased compared to a conventional radar, as shown in [18]. There it was also shown that from M TRX channels (that means every TX position is also an RX position), it is possible to synthesize a maximum number of $(M^2 + M)/2$ different antenna positions. For the presented case where $M=4$, this results in a total number of ten different virtual antenna positions. Another benefit that was recognized in [12] is that the MIMO system can be mapped to a conventional radar with virtual RX positions corresponding to the spatial convolution of the TX and RX phase centers. Besides the increase in the number of virtual channels, this leads to a larger virtual array aperture, and therefore, to a higher resolution if a standard beamformer is used. This advantage was exploited in [19]–[22]. In this study, we will make use of the antenna synthesis, and therefore, larger aperture, but further increase the aperture and achieve the maximum number of unique channels by designing a nonuniform array.

B. FMCW-Based Signal Model

The starting point for the algorithm development is the FMCW signal model for a single target. To simplify the derivations and to emphasize the MIMO idea, we first treat the static target case. Necessary extensions for the moving target

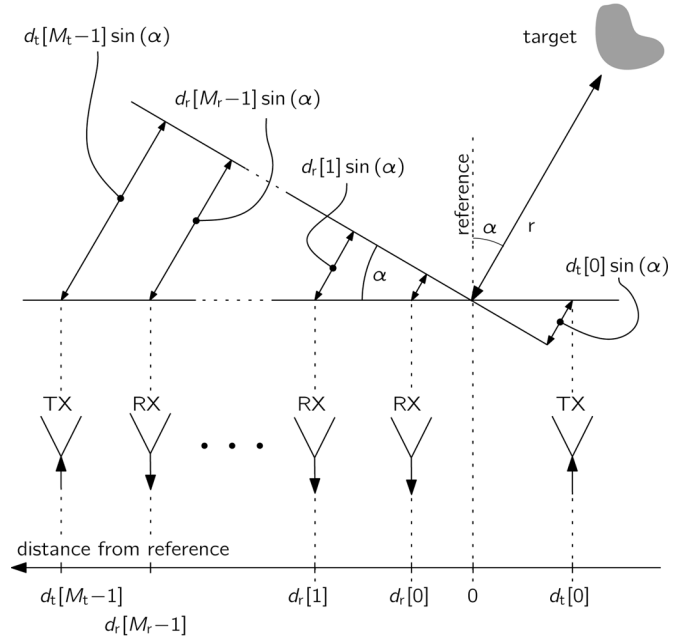


Fig. 4. Array configuration with multiple TXs and RXs used for the development of the MIMO signal model.

case will be introduced in Section IV-B.3. The time-varying frequency of the sinusoidal TX signal is defined as

$$f[n] = f_0 + \frac{B}{N}n \quad (1)$$

with $n = 0, 1, \dots, N-1$ being the discrete time index, N being the number of recorded samples, f_0 being the sweep starting frequency, and B being the effective sweep bandwidth. Assuming that the RX delivers complex valued data, a known result [23], [24] for the noiseless RX signal coming from a static target is

$$s[n] = AG(\alpha)e^{j(2\pi f[n](2r/c) + \phi_{\text{ref}})}. \quad (2)$$

Here, A represents the RX signal amplitude (which is dependent on the target's RCS, transmitted power, etc.), r is the target range, and c is the propagation velocity of the electromagnetic wave. Furthermore, ϕ_{ref} is an unknown reflection phase depending on target material properties, $G(\alpha)$ is the combined RX and TX antenna gain, and α is the target angle, as shown in Fig. 4. For an outline of the FMCW principle, it is referred to [23]. Equations (1) and (2) have been discretized using $t = nT_s$, where t is the continuous time and T_s is the sampling interval. This model can be extended to the MIMO case shown in Fig. 4. It can be observed that the wave's propagation time from a TX to the target and back to an RX consists of three parts. The first one is the delay due to the distance between the array reference point and the target

$$\tau_{\text{range}} = \frac{2r}{c}.$$

Assuming a plane wave (which means that the target is in the array's far field), the second delay or advance is due to the position $d_t[m_t]$ of TX m_t relative to the reference point

$$\tau_t[m_t] = \frac{d_t[m_t]}{c} \sin(\alpha)$$

and the third one is due to the position $d_r[m_r]$ of RX m_r

$$\tau_r[m_r] = \frac{d_r[m_r]}{c} \sin(\alpha).$$

Note that the distances to the reference point can be negative. Using these definitions, (2) can be extended to

$$s_{\text{MIMO}}[n, m_t, m_r] = e^{j2\pi f[n]\tau_t[m_t]} e^{j2\pi f[n]\tau_r[m_r]} s[n] \quad (3)$$

where $m_t = 0, 1, \dots, M_t - 1$ and $m_r = 0, 1, \dots, M_r - 1$ are the TX and RX indices and M_t and M_r denote the number of TXs and RXs, respectively. This equation gives an explanation as to how virtual antenna positions are synthesized. If only one TX would be used, each RX's signal is delayed according to the RX position. In a MIMO radar, the use of any extra shifted TX allows to use the same RXs, which now deliver signals that are additionally delayed due to the now changed TX position. These signals are equivalent to signals that would be outputted from RXs shifted by the same amount as the TX. Thus, under the prerequisite that signals from different TXs are separable at reception, the use of multiple TXs adds new virtual RX positions.

Another observation that can be made in (3) is that due to the signal delay or advance relative to the array reference caused by the TX, as well as the RX position, both the frequency and phase of $s_{\text{MIMO}}[n, m_t, m_r]$ depend on α , but it has to be stressed that the frequency variation along the receiving antennas due to the different angle-dependent round-trip delay times is very small (at least for moderate bandwidths and array apertures), and therefore, signals from targets located at the same range can be considered as being coherent (i.e., they have a fixed phase relation). This is the reason why a direct application of popular super-resolution algorithms without techniques like, for example, spatial smoothing [8] to the problem at hand, is not feasible.

C. Synthesis of Virtual Antennas Using TRX Multiplexing

As mentioned in Section III-A, it is necessary to distinguish the signals coming from different TX antennas at reception, which makes it possible to extract the information from each combination of the multiple TX and RX paths. This could be achieved, for example, via code or frequency division multiplexing, but in this study, we exploit the reconfigurability of the TRX and apply time division multiplexing (TDM). That means it is assured that during one FMCW ramp, only one TRX is working in the TRX mode, while all others are operating in the RX-only mode, and during one complete measurement cycle, each TRX is used as TRX once, as shown in Fig. 5. A big advantage of this approach is that signals of multiple TXs never interfere, and therefore it can be assured that the full 180° FOV will be maintained. If multiple TXs would be activated simultaneously, the resulting TX beam pattern would have zeros in

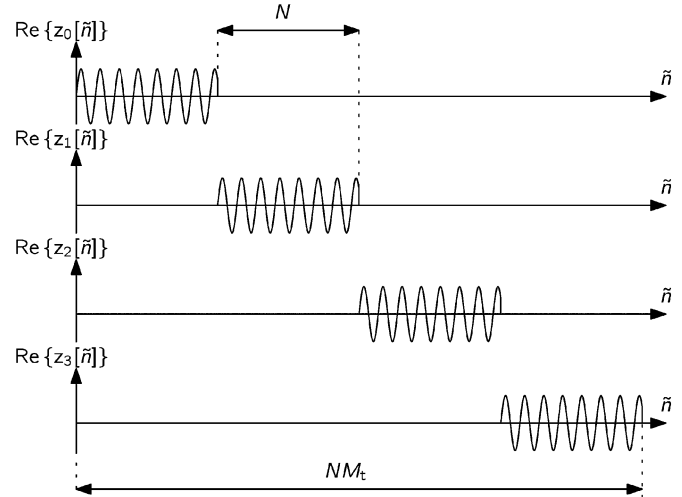


Fig. 5. Angle-independent virtual baseband signals occurring due to the TDM MIMO principle.

certain directions, and therefore, no target could be detected in this part of the space.

The signal (2), which solely contains the range information, is used to build the vector

$$\mathbf{s} = [s[0] s[1] \dots s[N-1]]^T. \quad (4)$$

The TDM principle is modeled via a vector $\mathbf{z}_{m_t} \in \mathbb{C}^{NM_t \times 1}$ containing (4) padded with zeros to account for the sequential activation of the TXs according to Fig. 5. Thus, the virtual baseband signal occurring due to the TX with index m_t is written as

$$\mathbf{z}_{m_t} = [\mathbf{0}_{1 \times m_t N} \mathbf{s}^T \mathbf{0}_{1 \times (M_t - 1 - m_t) N}]^T \quad (5)$$

where $\mathbf{0}_{u \times v}$ denotes a zero matrix of dimension $u \times v$. Note that due to the zero padding, the length of the signal has increased to $\tilde{N} = NM_t$ with the new time index $\tilde{n} = 0, 1, \dots, \tilde{N} - 1$ (cf. Fig. 5). Therefore, the varying frequency of the TX signals is redefined to

$$\tilde{f}[\tilde{n}] = f_0 + \frac{B}{N} \left(\tilde{n} - \left\lfloor \frac{\tilde{n}}{N} \right\rfloor N \right)$$

with $\lfloor \cdot \rfloor$ denoting the floor operator. This is needed to mathematically describe that every TX starts its sweep at f_0 . Using the above definitions, it is possible to define a snapshot vector containing the samples from all TXs at a time instant \tilde{n}

$$\mathbf{y}[\tilde{n}] = [\mathbf{z}_0[\tilde{n}] \mathbf{z}_1[\tilde{n}] \dots \mathbf{z}_{M_t-1}[\tilde{n}]]^T.$$

Defining the TX steering vector as

$$\mathbf{a}_t(\tilde{n}, \alpha) = [e^{j2\pi \tilde{f}[\tilde{n}] \tau_t[0]} e^{j2\pi \tilde{f}[\tilde{n}] \tau_t[1]} \dots e^{j2\pi \tilde{f}[\tilde{n}] \tau_t[M_t-1]}]^T \quad (6)$$

allows to write the baseband signal due to the multiple TXs as $\mathbf{a}_t^T(\tilde{n}, \alpha) \mathbf{y}[\tilde{n}]$. The RX array possesses the receive steering vector

$$\mathbf{a}_r(\tilde{n}, \alpha) = [e^{j2\pi \tilde{f}[\tilde{n}] \tau_r[0]} e^{j2\pi \tilde{f}[\tilde{n}] \tau_r[1]} \dots e^{j2\pi \tilde{f}[\tilde{n}] \tau_r[M_r-1]}]^T.$$

This allows the complete description of the MIMO signal model as

$$\mathbf{s}_{\text{MIMO}}[\tilde{n}] = \mathbf{a}_r(\tilde{n}, \alpha) \mathbf{a}_t^T(\tilde{n}, \alpha) \mathbf{y}[\tilde{n}] = \mathbf{A}(\tilde{n}, \alpha) \mathbf{y}[\tilde{n}] \quad (7)$$

which contains the information of all TX–RX path combinations at the time instance \tilde{n} . Contrary to a standard phased array, this leads to a steering matrix $\mathbf{A}(\tilde{n}, \alpha) \in \mathbb{C}^{M_r \times M_t}$ where

$$[\mathbf{A}(\tilde{n}, \alpha)]_{k,l} = [\mathbf{a}_r(\tilde{n}, \alpha)]_k [\mathbf{a}_t(\tilde{n}, \alpha)]_l = e^{j2\pi\tilde{f}[\tilde{n}](\tau_r[k] + \tau_t[l])} \quad (8)$$

rather than the steering vector resulting from a conventional radar. Here, \mathbf{A} contains all the paths from TX l to RX k . As can be seen from (3), using multiple TXs and RXs allows to generate a larger array with multiple RXs positioned virtually at distances according to the sum of TX and RX distance to the reference point. In the presented case with four TRX channels, (8) has 16 entries, but since the positions of TX and RX coincide for the presented TRX structure, only ten different virtual RX positions can be synthesized because $[\mathbf{A}(\tilde{n}, \alpha)]_{k,l} = [\mathbf{A}(\tilde{n}, \alpha)]_{l,k}$. Of course, the information coming from the remaining redundant positions is still valuable since at least parts of the noise in these channels can be modeled as being independent to the noise influencing the other channels. Therefore, the redundant information can be used to reduce the negative effect of these noise components. Furthermore, this information is valuable in the moving target case, as will be shown in Section IV-B.3. To achieve the maximum number of virtual antenna positions, it is necessary to deviate from a standard uniform array arrangement because using a uniform array with interelement spacing d would lead to the relation

$$\tau_r[k] + \tau_t[l] = (k+l) \frac{d}{c} \sin(\alpha)$$

and therefore to only seven different virtual antenna positions because $(k+l) \in \{0, 1, \dots, 6\}$. Thus, in this study, we will make use of a nonuniform array, which allows the virtualization of the maximum possible ten virtual antenna positions. An additional advantage stemming from the use of such an array configuration is that it allows antenna distances between the physical array elements exceeding $\lambda/2$ without causing grating lobes [25] because virtual distances between synthesized antennas can be smaller than $\lambda/2$ if the physical spacing is chosen accordingly. This leads to an additional increase of the array's aperture, and therefore, angular resolution.

The very general model (7) can be used for a broad range of simultaneously transmitted signals regardless of the multiplexing technique and allows to directly apply results from, for example, [18], [26], and [27] to the problem at hand. Noticing that for every \tilde{n} , only one element of $\mathbf{y}[\tilde{n}] \neq 0$ due to the TDM allows a considerable simplification. As can be seen from (7), at each time instance, only one column of \mathbf{A} contributes to \mathbf{s}_{MIMO} ,

which means the signals caused by the different TXs can be perfectly separated. Therefore, (7) can be rewritten defining a virtual array with the modified MIMO steering vector

$$\mathbf{a}(\tilde{n}, \alpha) = \text{vec}(\mathbf{A}(\tilde{n}, \alpha)) \quad (9)$$

where $\text{vec}(\cdot)$ denotes the operator of stacking the columns of a matrix on top of each other. Now $\mathbf{a}(\tilde{n}, \alpha)$ is similar to the steering vector of a standard array, but its length is increased due to the virtual antennas synthesized by the MIMO principle. Since it was assumed in (2) that the target does not move during a measurement cycle, the time delays due to the TX multiplexing can be neglected, and therefore, the RX signal snapshot vector $\mathbf{x}[n]$ can be written in a form as if the TXs would have been activated simultaneously. To notationally simplify the further discussions, we now use the time index of a single FMCW ramp n again. This allows us to write

$$\mathbf{x}[n] = \mathbf{a}(n, \alpha) s[n] + \mathbf{u}[n]. \quad (10)$$

To account for a multitarget scenario, we define a noise plus interference term

$$\mathbf{u}[n] = \sum_{p=0}^{P-1} \mathbf{a}(n, \alpha_{u,p}) s_{u,p}[n] + \mathbf{w}[n] \quad (11)$$

containing noise $\mathbf{w}[n]$ and P unwanted signals $s_{u,p}[n]$ coming from directions $\alpha_{u,p}$ other than α . Note that due to the MIMO principle, we now have virtually $M_M = M^2$ RX antennas with $(M^2 + M)/2$ different antenna positions.

IV. SIGNAL PROCESSING

A. Delay-and-Sum Beamformer

A well-known way to recover $s[n]$ coming from direction α is the so-called delay-and-sum or conventional beamformer. As the name implies, the phase shift of the signal of each channel due to the propagation delay along the array is compensated according to (9). In this way, the signals from the RX antennas are aligned and then summed up to form the estimate $\hat{s}_\alpha[n]$ for $s[n]$ coming from α

$$\hat{s}_\alpha[n] = \frac{1}{M_M} \mathbf{a}^H(n, \alpha) \mathbf{x}[n]. \quad (12)$$

Although (2) was developed under the assumption of a single target, (12) is also usable for multiple targets, as shown in [28, Ch. 6]. Equation (12) is only an approximate solution for the complete multitarget model, but inserting (10) and (11) into (12) leads to

$$\hat{s}_\alpha[n] = s[n] + \frac{1}{M_M} \sum_{p=0}^{P-1} \mathbf{a}^H(n, \alpha) \mathbf{a}(n, \alpha_{u,p}) s_{u,p}[n] + \frac{1}{M_M} \mathbf{a}^H(n, \alpha) \mathbf{w}[n]. \quad (13)$$

Therefore, it is obvious that (13) works in the single target ($s_{u,p}[n] = 0$) and noiseless ($\mathbf{w}[n] = \mathbf{0}$) case. In multitarget scenarios, the term $\mathbf{a}^H(n, \alpha) \mathbf{a}(n, \alpha_{u,p})$ in (13) is relevant. For targets with a large enough angular separation (i.e., separation larger than the Rayleigh resolution limit),

$\mathbf{a}^H(n, \alpha) \mathbf{a}(n, \alpha_{u,p}) \ll M_M$ [4], [29], and thus, signals coming from other than the wanted direction are suppressed. This means that (12) can also be used in the case of multiple targets, even if they are completely coherent. The separation needed to angularly resolve targets is related to the arrays aperture [4], [30]. For a standard uniform half-wavelength spaced array, this resolution capability is very poor due to the small array aperture, but due to the use of sparse arrays and the MIMO technique, the total number of resolvable targets and their minimum necessary angular separation that guarantees resolvability can be improved to a large extent. This allows the application of the computationally efficient and robust conventional beamforming method (12) for many practical applications. Furthermore, the use of the conventional beamformer has the positive side effect that the number of targets can be inherently estimated from the number of peaks in the resulting cost function. These advantages and the algorithm's insensitivity against coherent signals, which need special treatment in many of the often used superresolution algorithms [7], [8], make this algorithm perfectly suitable for our further investigations.

B. Combined Range and Angle Estimation

1) Derivation of a 2-D Power Distribution: It is possible to estimate the target's range from (2). In conjunction with the beamformer defined in (12), it is therefore possible to calculate a 2-D power distribution over all angles and ranges. A discrete Fourier transform (DFT) is applied to (12), which allows to calculate an estimate for the power reflected from a certain 2-D position in polar coordinates

$$\left| \hat{A}(r, \alpha) \right|^2 = \left| \frac{1}{N} \sum_{n=0}^{N-1} \hat{s}_\alpha[n] e^{-j(2\pi f[n](2r/c))} \right|^2. \quad (14)$$

The power distribution calculated via (14) can be used for target detection and localization by using the position of power peaks that exceed a certain threshold as estimates for the target location. Inserting (12) into (14) yields

$$\left| \hat{A}(r, \alpha) \right|^2 = \left| \frac{1}{NM_M} \sum_{n=0}^{N-1} \sum_{m=0}^{M_M-1} x[n, m] \times e^{-j2\pi f[n]((2r/c)+(d[m]/c) \sin(\alpha))} \right|^2 \quad (15)$$

where $d[m]$ is a virtual antenna distance according to the entries in (9). To directly calculate (15), the implementation based on the chirp z -transform [31], as shown in [25], can be used, which is valid for chirps with any B .

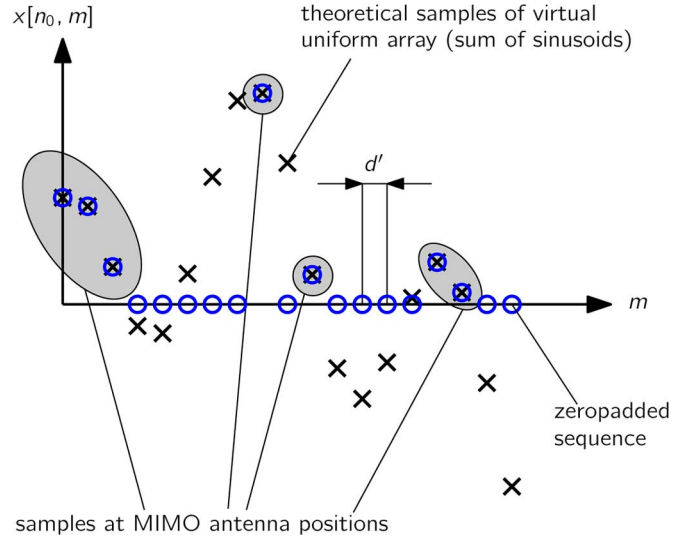


Fig. 6. Depiction of the applied zero padding to generate a virtual uniform array, which allows an efficient algorithm implementation using an FFT.

2) Efficient Calculation of the 2-D Power Distribution: For a small B , (15) can be approximately calculated much faster by a 2-D fast Fourier transform (FFT). To achieve this, the inner and outer sum in (15) need to be separated. Inserting (1) into (15) and omitting the normalization factor $1/(NM_M)$ to simplify the notation leads to the cost function shown in (16) at the bottom of this page. The approximation used to derive (16) is the narrowband assumption, which assumes that the phase variation along the array's aperture due to B is much smaller than the phase variation due to f_0 , which is fulfilled if $B \ll f_0$. This allows to separate the parts of the exponential term that depend on n and m . Since this study deals with nonuniform arrays, the inner sum—although separated—cannot be directly calculated using an FFT. Although fast algorithms to calculate a nonuniform DFT are available [32], they are often based on additional approximations and are computationally not as efficient as an FFT. Thus, we propose the use of a second step, where a virtual uniform array is constructed by padding the data with zeros, as shown in Fig. 6. This technique allows to write the virtual antenna distances as multiples of a new summation variable m' while not changing the result of the inner sum. Note that the uniform antenna spacing d' of the virtual array has to be chosen correctly so that all $d[m]$ are contained in the summation. It is important to keep this in mind in the design of the array to ensure that d' does not become too small because, in this case, the number of elements M' in the virtual uniform array becomes

$$\begin{aligned}
 J(r, \alpha) &= \left| \sum_{n=0}^{N-1} \sum_{m=0}^{M_M-1} x[n, m] e^{-j2\pi((B/N)(2r/c)n + (f_0 + (B/N)n)(d[m]/c) \sin(\alpha))} \right|^2 \\
 &\approx \left| \sum_{n=0}^{N-1} e^{-j2\pi(B/N)(2r/c)n} \sum_{m=0}^{M_M-1} x[n, m] e^{-j2\pi f_0(d[m]/c) \sin(\alpha)} \right|^2 \quad (16)
 \end{aligned}$$

very large. If M' is becoming too big, the computational advantage of the proposed method can be severely reduced. With the definitions of the virtual uniform array, (16) can be written as

$$J(r, \alpha) = \left| \sum_{n=0}^{N-1} e^{-j(2\pi\psi_r(r)n)} \sum_{m'=0}^{M'-1} x'[n, m'] \times e^{-j(2\pi\psi_\alpha(\alpha)m')} \right|^2 \quad (17)$$

with x' being the zero-padded data,

$$\psi_r(r) = \frac{B}{N} \frac{2r}{c} \quad (18)$$

being the normalized range-dependent temporal frequency and

$$\psi_\alpha(\alpha) = f_0 \frac{d'}{c} \sin(\alpha) \quad (19)$$

being the angle-dependent spatial frequency. Note that no interpolation of the data is necessary to create the virtual uniform array. Only zeros are inserted at positions where no antenna is present, which allows to calculate (16) efficiently via (17) using an FFT. Since the two sums are exchangeable, it is possible to first evaluate an FFT in one dimension (e.g., range, i.e., along all n) and then process only the result in the other dimension corresponding to locations of interest (e.g., with high power). This is one possibility to further reduce the computational burden. Another effect can be exploited noting that d' usually will be much smaller than $\lambda/2$, which leads to the behavior that the spatial FFT will deliver results for angles $|\alpha| > 90^\circ$, but these results are only replicas of the original spectrum, and therefore, contain no new information. Thus, it is sufficient to calculate the spatial FFT in a region corresponding to the wanted FOV, which can efficiently be realized using the chirp z -transform. With these presented methods, it is possible to calculate the 2-D cost function with very low computational power.

3) *Moving Target Case:* As already mentioned at the beginning of Section III-B, the models used hitherto assume static targets only. To include possible target movement into the signal processing, some extensions are necessary. First, (2) has to be changed to include the Doppler shift into the signal model. The new signal model for a moving target becomes $s_{\text{mov}}[n] = s[n]e^{j2\pi\psi_D n}$, where

$$\psi_D = \frac{2v_r}{c} f_0 T_s \quad (20)$$

denotes the normalized frequency shift due to the Doppler effect caused by the radial target velocity v_r . Thus, the use of (17) leads to a radial displacement

$$\Delta r = v_r f_0 T_s \frac{N}{B} = v_r f_0 \frac{T_{\text{sweep}}}{B} \quad (21)$$

of the target position estimates. It is possible to estimate v_r , e.g., by using combinations of multiple upchirps/downchirps with varying frequency ramp slopes. Since the estimation of target velocities is beyond the scope of this study, we refer to the existing literature, e.g., [33]. The second necessary change occurs because of the sequential TX activation. Due to the target movement, the phase relations of the signals at the virtual antennas

change during a measurement cycle. Thus, (12) is not directly applicable to the moving target case, but the information about the changing phase relations is contained in the signals from the redundant antenna positions. The result of the calculation of the range DFT at the m th antenna is

$$X_m(r) = \sum_{n=0}^{N-1} x[n, m] e^{-j2\pi(B/N)(2r/c)n}. \quad (22)$$

Considering a static target situation, the phases of the redundant signals are equal, which can be written as

$$\arg(X_k(r)) = \arg(X_{M_t k}(r)), \quad k = 1, 2, \dots, M_t - 1. \quad (23)$$

Equation (23) also holds for all other redundant signals, but we use only the first $M_t - 1$ here for the sake of simplicity. For moving targets, a certain phase shift occurs between the signals measured from different TX activations. If it is assumed that the change in frequency due to the target motion can be neglected, we can write

$$\arg(X_k(r)) + \Delta\phi_k(r) = \arg(X_{M_t k}(r)), \quad k = 1, 2, \dots, M_t - 1 \quad (24)$$

which is fulfilled for targets staying in the same range bin during one measurement cycle. This is comparable to the narrowband assumption used in (16). Note that no special assumptions about the target movements have been made. $\Delta\phi_k(r)$ is a result from the displacement of targets from one FMCW ramp to another, which can be caused both by radial, as well as tangential movement. The estimation of $\Delta\phi_k(r)$ is now possible by calculating the phase differences

$$\hat{\Delta\phi}_k(r) = \arg(X_{M_t k}(r)) - \arg(X_k(r)), \quad k = 1, 2, \dots, M_t - 1. \quad (25)$$

These estimates can then be applied to the measured data to compensate the motion caused phase shifts via

$$X_{m, \text{comp.}}(r) = X_m(r) e^{-j\hat{\Delta\phi}_l(r)} \quad (26)$$

where $l = m \bmod M_t$ and $m = 0, 1, \dots, M_M - 1$. The first TX antenna is used as phase reference, thus, $\Delta\phi_0(r) = 0$. After zero padding according to Section IV-B.2, the modified data can directly be used in (17) to calculate the 2-D cost function

$$J(r, \alpha) = \left| \sum_{m'=0}^{M'-1} X_{m', \text{comp.}}(r) e^{-j(2\pi\psi_\alpha(\alpha)m')} \right|^2. \quad (27)$$

Due to the use of the first TX antenna as a phase reference, the data compensated in this way will be referred to the first TX, which means that the calculated angular target positions will be the positions corresponding to the beginning of a measurement sequence. The applicability of the presented phase compensation will be shown in Section VII-B.1.

C. Array Calibration

The previous discussions are only valid under the assumption that the steering vector is known perfectly, but in practice, this

knowledge is seldom available since due to manufacturing inaccuracies and design necessities additional delays are introduced into the signal path of each antenna. If the phase shifts originating from these path lengths are equal for each antenna, this does not influence the angle measurement, as the operation of taking the absolute value in (15) eliminates such phase shifts, but different unknown phase shifts at each antenna prohibit the direct use of (15). Fortunately, here again the TDM-MIMO principle allows a simple solution of this problem. Since each virtual channel can be considered as a single radar sensor, range measurements to a known reference target conducted with each channel allow the determination and correction of the different path lengths, but a standard range measurement based on the evaluation of the frequency in (2) (as it is usually carried out in FMCW radar sensors) is not sufficient to deliver a result accurate enough to compensate the phase errors. This can be shown by calculating the best achievable range accuracy stated by the Cramér-Rao lower bound (CRLB). The lowest achievable range standard deviation independent of the used signal processing algorithm can be derived from the CRLB for frequency estimation given in [29] to

$$\sigma_{\hat{r},\text{freq}} \geq \sqrt{\frac{3c^2}{2(2\pi)^2 NB^2\eta}}. \quad (28)$$

Considering the case of an FMCW radar with $f_0 = 77$ GHz, $B = 1$ GHz, and $N = 1000$ operating at an SNR of $\eta = 10$ dB, (28) gives a lower limit of $\sigma_{\hat{r},\text{freq}} \geq 0.59$ mm, which is equivalent to a phase shift in free space of 54° . This accuracy is clearly insufficient for a successful calibration of the array. One possibility to reduce this variance would be simply averaging many measurements, but observing (1) and (2) reveals that not only the frequency components contained in $s[n]$ contain information about the target range, but also the phase of $s[n]$. The CRLB for the range standard deviation based on phase estimation can also be calculated following [29] to

$$\sigma_{\hat{r},\text{phase}} \geq \sqrt{\frac{c^2}{2(2\pi)^2 N f_0^2 \eta}}. \quad (29)$$

Using the same parameters as in the previous example, (29) gives a lower limit of $\sigma_{\hat{r},\text{phase}} \geq 4.4$ μm , which is equivalent to a phase shift in free space of only 0.4° . Although this information is very accurate, it can clearly not be used for range measurements because of the unknown target reflection phase together with the 2π ambiguity of phase measurements, but it is perfectly suited for the use in the array calibration because the reflection phase is equal for each antenna, and therefore, vanishes in the evaluation. This also implies that the range of the reference target needs not to be known because a range variation leads only to identical phase shifts at each antenna. Furthermore, the 2π -ambiguities are also irrelevant because in (15) the phase information is used in the argument of a complex exponential function, and thus, the addition of multiples of 2π does not influence the result. Note that (29) does not depend on B . Therefore, the phase calibration can be carried out with a narrowband signal without influencing the achievable accuracy. That means that if B is chosen properly, it can be assured that the narrowband assumption is fulfilled during the calibration process.

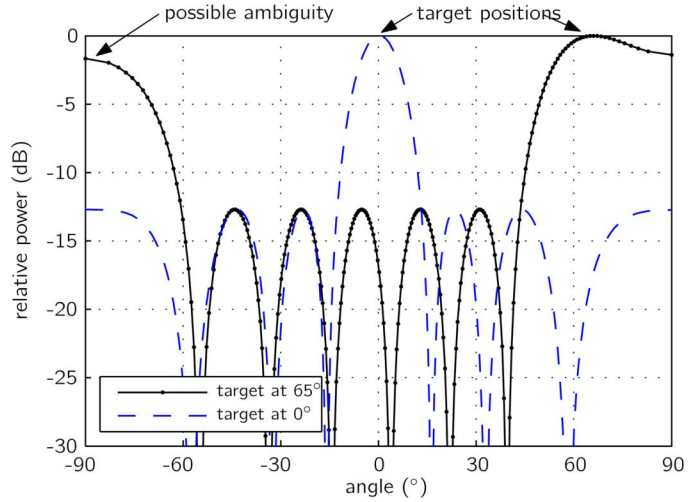


Fig. 7. Response of a standard half-wavelength spaced array with seven elements to targets at 0° and 65° with an equisidlobe window according to [34] with an SLL of -13 dB. It can be seen that the target at 65° can cause an ambiguity at -90° due to the nonzero mainbeam width if the measurement is corrupted by noise.

V. ARRAY DESIGN

The results from Sections III and IV show how a MIMO radar in combination with an arbitrary nonuniform array can be used to localize targets in two dimensions using computationally efficient FFTs. This section deals with the design of the array, namely, the antenna positions and weighting (windowing) functions for sidelobe control. From antenna array theory, it is known that an array has to fulfill certain properties to be usable for direction finding applications. Usually it is assumed that the array elements are equally spaced with a distance of $\lambda/2$. In this case, the sampling theorem is fulfilled in the spatial domain and ambiguities (grating lobes) occur at [4, pp. 50–51]

$$\sin(\alpha_{\text{amb}}) = \sin(\alpha) + 2i, \quad \text{for } i = \pm 1, \pm 2, \dots$$

where α_{amb} is the position of the grating lobe. It can be seen that for targets located at 90° , the first grating lobe occurs at -90° and vice versa. Therefore, the $\lambda/2$ spacing is not sufficient if beamforming for the full 180° FOV is desired since targets near $\pm 90^\circ$ can cause ambiguities due to the nonzero beamwidth. An example for this behavior is depicted in Fig. 7. For comparative purposes, a uniform array with seven elements was used, which can be synthesized from a four-channel TRX module with equidistant array element spacing. A Dolph–Chebyshev spatial windowing function with a sidelobe level (SLL) of -13 dB was used for the uniform array.

Applying windows to the data prior to the evaluation of (17) can be written as

$$\begin{aligned} J_{\text{win}}(r, \alpha) &= \left| \sum_{n=0}^{N-1} e^{-j2\pi\psi_r(r)n} \sum_{m'=0}^{M'-1} x'_{\text{win}}[n, m'] e^{-j2\pi\psi_\alpha(\alpha)m'} \right|^2. \end{aligned} \quad (30)$$

Here,

$$x'_{\text{win}}[n, m'] = w_r[n] w_\alpha[m] x'[n, m']$$

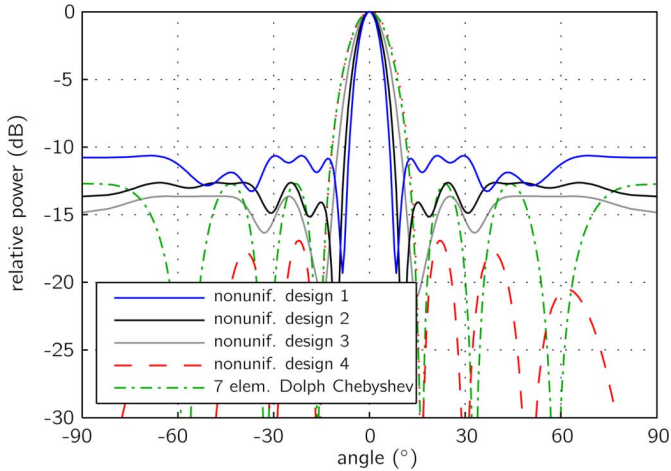


Fig. 8. Comparison of the response from different nonuniform arrays with a seven-element uniform array to a target positioned at 0° . The tradeoff between SLL and mainbeam width is clearly visible.

is the modified data with windows that allow a tradeoff between the beamwidth and SLL in the range dimension via $w_r[n]$ and in the angular dimension via $w_\alpha[m]$. This study only deals with the design of $w_\alpha[m]$ since the temporal windowing is straightforward due to the known windowing theory in the application of the DFT to uniformly sampled signals. In the uniform array case, these windows can be designed, e.g., to achieve the minimum possible beamwidth for a given SLL, as shown in [34], for array element spacings $d \geq \lambda/2$ and in [35] also for $d < \lambda/2$, where the latter is only usable for an odd number of array elements. The patterns from Fig. 7 have been designed using the method described in [34]. Unfortunately, no analytic solution is available to calculate the weight vector and antenna positions for arbitrary spaced arrays. Even for a given array, it is not straightforward to find the optimum weight vector in terms of SLL and mainbeam width. Here, we chose the approach presented in [36], which uses theory from the field of convex optimization. Software available from [37] was used to solve the optimization problem. This approach allows the calculation of optimal weights for an arbitrary array with a minimized SLL outside a given mainbeam width, where it is guaranteed that the found solution is the global optimum. Furthermore, the sidelobe region can be extended so that the entire scanning range from -90° to 90° is available without grating lobes. Since only three antenna spacings need to be considered in this study, it is feasible to search the entire parameter space defined by minimal and maximal antenna spacings for an optimal solution to the element positioning problem. In the presented examples, the search was carried out for antenna distances $1.7 \text{ mm} \leq \Delta \leq 10 \text{ mm}$ in steps of 0.1 mm. This step size also ensures that the zero-padding method described in Section IV-B is applicable to the problem without increasing the number of virtual samples too much. Some examples from the results are shown in Fig. 8. The tradeoff between beamwidth and SLL is also clearly visible for the nonuniform array pattern. The nonuniform MIMO array has a smaller beamwidth for a given SLL as the seven-element uniform array used here for comparison. This is a big advantage regarding the resolvability

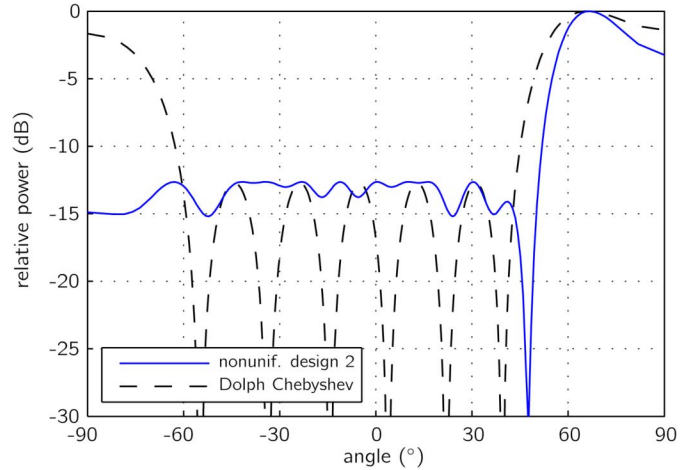


Fig. 9. Comparison of the response from a seven-element array with Dolph-Chebyshev weighting and the optimized nonuniform array #2 to a target positioned at 65° . It is clearly visible that the nonuniform array does not suffer from ambiguity problems.

TABLE I
DIFFERENT ARRAY CONFIGURATIONS LEADING TO THE BEST ACHIEVABLE SLL AT A CERTAIN MAINBEAM WIDTH α_3 dB

design #	Δ_1	Δ_2	Δ_3
1	3.7 mm $\approx 0.9\lambda$	7.4 mm $\approx 1.9\lambda$	1.8 mm $\approx 0.5\lambda$
2	1.8 mm $\approx 0.5\lambda$	5.4 mm $\approx 1.4\lambda$	3.6 mm $\approx 1.0\lambda$
3	3.4 mm $\approx 0.9\lambda$	5.1 mm $\approx 1.3\lambda$	1.7 mm $\approx 0.5\lambda$
4	1.7 mm $\approx 0.5\lambda$	3.5 mm $\approx 0.9\lambda$	1.7 mm $\approx 0.5\lambda$

TABLE II
BEST ACHIEVABLE SLL AT A CERTAIN MAINBEAM WIDTH α_3 dB

design #	α_3 dB	SLL
1	$\pm 3.7^\circ$	-10.7 dB
2	$\pm 4.4^\circ$	-12.7 dB
3	$\pm 5.4^\circ$	-13.7 dB
4	$\pm 6.8^\circ$	-17.4 dB

of targets throughout the entire FOV. Regardless of the target position, the beamwidth of the nonuniform array is always smaller than that of the uniform one because the broadening of the beams due to the nonlinear relation (19) between the spatial frequency and the target angle affect both array types equally. Another distinct feature of the nonuniform arrangement is that unlike the standard $\lambda/2$ spaced array, the nonuniform array was designed to avoid ambiguities also for targets located up to $\pm 90^\circ$. The comparison shown in Fig. 9 clearly reveals that, in this case, the nonuniform array designed in this study clearly outperforms its uniform counterpart. Tables I and II show array configurations and numerical values for the corresponding mainbeam width and SLL obtained with the described method. Note that the optimization of the SLL was carried out for the full 180° FOV, thus the SLL values from Table II are valid for the entire scanning range. Table III gives the resulting weighting functions for the presented array configurations (indexed for increasing virtual antenna distances).

VI. PROTOTYPE HARDWARE

To test the developed TRX as well as the target localization algorithm in different measurement applications, a radar front-end based on the array design number two was realized. This array was chosen because it has a 3-dB mainbeam width smaller

TABLE III
 OPTIMIZED WEIGHTS FOR THE FOUR PRESENTED ARRAY DESIGNS

design #	$w_\alpha[0]$	$w_\alpha[1]$	$w_\alpha[2]$	$w_\alpha[3]$	$w_\alpha[4]$
1	0.0476	0.0861	0.1348	0.1128	0.0669
2	0.0810	0.1533	0.0908	0.0794	0.1296
3	0.0427	0.0995	0.1391	0.1219	0.0978
4	0.0980	0.0909	0.1162	0.1252	0.0697

design #	$w_\alpha[5]$	$w_\alpha[6]$	$w_\alpha[7]$	$w_\alpha[8]$	$w_\alpha[9]$
1	0.0353	0.1262	0.1666	0.1630	0.0606
2	0.0495	0.1005	0.1281	0.1265	0.0612
3	0.1734	0.1007	0.0677	0.1008	0.0565
4	0.0697	0.1252	0.1162	0.0909	0.0980

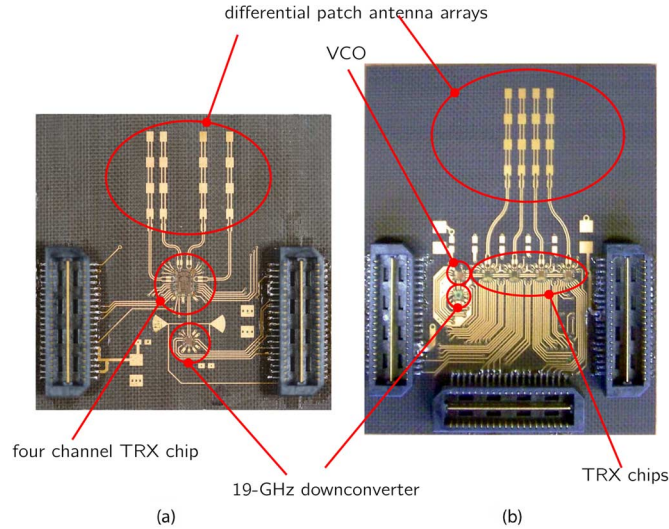


Fig. 10. (a) Photograph showing the realized nonuniform frontend consisting of the four channel TRX TRX and a 19-GHz downconverter used for the offset loop implementation. The overall size of the board is 4 cm \times 4 cm. (b) photograph showing the frontend with uniform array configuration consisting of a VCO, four single-channel TRX chips, and the 19-GHz downconverter. The overall size of this board is 4 cm \times 5 cm.

than 10° and an SLL comparable to that of an uniform array with a rectangular spatial window function. To allow a space-saving design, baluns have been avoided and the frontend printed circuit board (PCB), therefore, was equipped with four differential series-fed patch antennas [38]. The TRX's on-chip frequency divider is used in conjunction with a 19-GHz downconverter [39] to implement an offset loop, as presented in [40]. This configuration allows the generation of low phase noise and linear frequency ramps. To collect the measurement data and control the blocks for signal generation and A/D conversion, a base-band part using a field-programmable gate array (FPGA) as the central element, as presented in [41], was used. The signal processing for the presented measurements took place on a PC. The left photograph of Fig. 10 shows the realized RF frontend. For comparative purposes, a system using a $\lambda/2$ spaced uniform array configuration was used. This frontend shown in the right photograph of Fig. 10 is realized using multiple chips, but with the same TRX capabilities and the same offset loop configuration as the presented single-chip solution. Thus, according to Section III-C, it is possible to synthesize seven virtual antennas from the four physically existing uniformly arranged array elements.

 TABLE IV
 MEASUREMENT AND SYSTEM PARAMETERS

f_0	B	T_{sweep}	N	ADC resolution
75 GHz	2 GHz	2 ms	2000	12 bit

VII. MEASUREMENTS

To verify the system performance in different scenarios, multiple measurements have been made. First, measurements to evaluate parameters like achievable accuracy and multitarget capabilities have been performed in an anechoic chamber. Thus, influences from the environment could be minimized to a level that allows to draw conclusions about the achievable system performance. Second, results from outdoor measurements show the applicability of the proposed radar concept and its algorithms to real-world applications.

A. Description of the Measurement Procedure

All measurements have been conducted with the parameters given in Table IV. A calibration, as described in Section IV-C, was performed during the first measurements using a single corner cube (CC) as a reference target to determine the phase offset of each channel. This calibration data was used throughout the entire presented measurements to demonstrate the robustness of the proposed principle against varying environmental conditions.

B. Measurement Results

1) Anechoic Chamber:

a) Ambiguity Avoidance and Calibration: The first system test was carried out using a single CC as the target. The shorter edges of the triangles building the reflector have a length of 70 mm, which leads to an RCS of 8.2 dBm according to [42, p. 89]. First, the target was positioned at a distance of 1.9 m at an angle of 0° . For this configuration, 100 measurements have been taken using both the nonuniform and uniform system. This data was used to calculate the calibration data for both systems. The results using this calibration data for the 100 measurements are shown in Fig. 11. Both systems correctly detect the highest power at the target position of 0° . The MIMO array with the uniform antenna arrangement has a broader mainbeam compared to its nonuniform counterpart, as expected from the simulations (cf. Fig. 8). Next, the target was moved to an angle of 65° to check the validity of the calibration data for varying angles and to show the ambiguity problems that can occur using an uniformly $\lambda/2$ spaced array. Again, 100 measurements have been taken. The results using the calibration data from the first measurements are depicted in Fig. 12. It can be seen from Fig. 12 that both beams are broadened, as expected from (19). Nevertheless, the beam resulting from the nonuniform arrangement is narrower than the one resulting from the uniform array. Furthermore, the uniform array suffers from ambiguity problems due to the leakage of signal power into the region of negative angles. Comparing the resulting beampattern to the simulated curve in Fig. 8 shows a 2-dB increase in the SLL of the nonuniform array. Thus, for applications with high-accuracy requirements, it might be necessary to introduce an angle-dependent calibration that possibly corrects wrong element spacings caused by

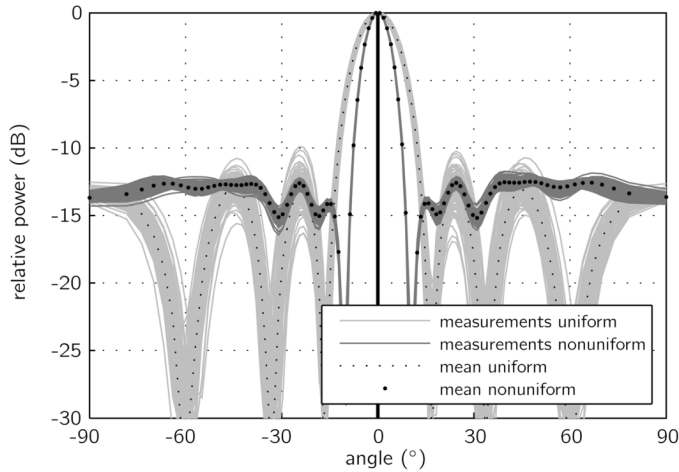


Fig. 11. Comparison of the measurement results of a single CC positioned at an angle of 0° using the nonuniform, as well as uniform array.

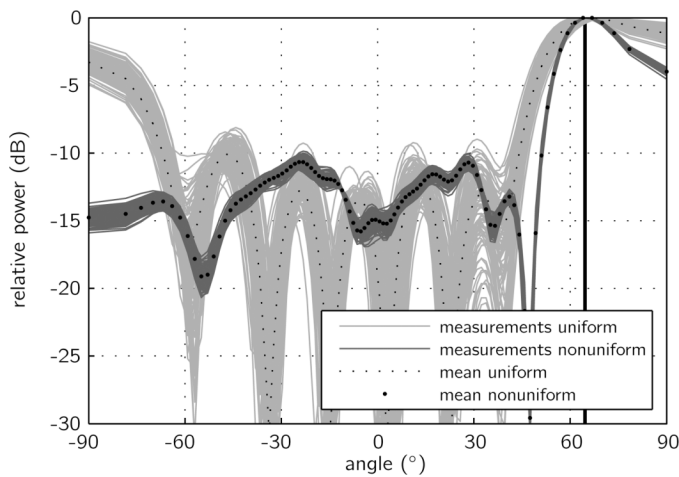


Fig. 12. Comparison of the measurement results of a single CC positioned at an angle of 65° achieved using the nonuniform, as well as uniform array. The uniform array suffers from ambiguity problems due to the leakage of signal power into the region of negative angles.

fabrication tolerances and includes mutual coupling or other effects that are not covered by the simple assumption of unequal phases at the RX channels.

b) Measurements With Multiple Targets Located at Equal Radial Positions: After it was confirmed that both arrays perform as expected, the increase in angular resolution was tested using two CCs. First, two targets of the same size as in the single target example have been placed at angles of 7° and -7° , both at a distance of 1.9 m. As can be seen from Fig. 13, this arrangement is close to the resolution ability of the nonuniform array. The result achieved with the uniform array does not reveal the two targets, but only one peak with the maximum in between the two true target positions. As a second example, two CCs have been placed at a distance of 1.9 m with angular positions of 0° and 45° , respectively. The results for this scenario are shown in Fig. 14. In this case, the power returned from the CC positioned at 45° is smaller than that from the target at 0° because of the (broad, but toward $\pm 90^\circ$ still decreasing) beam pattern of the single array elements. From Fig. 14, it can be seen that the

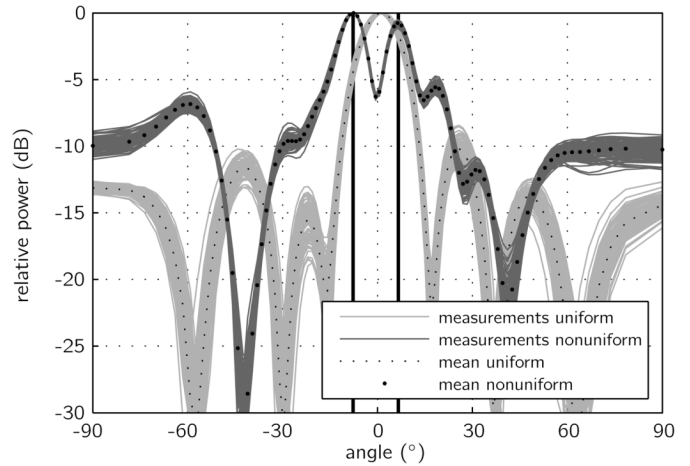


Fig. 13. Measurement results of two equally sized CCs positioned at angles of 7° and -7° . The nonuniform array is capable of resolving the two targets, whereas the uniform array shows only one peak in the estimated angular power distribution.

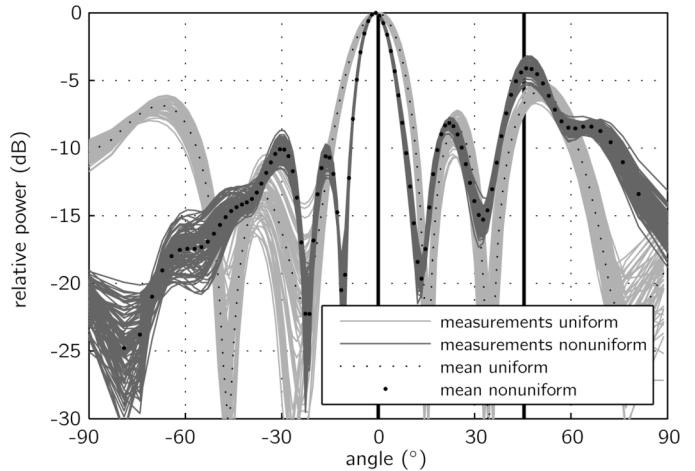


Fig. 14. Measurement results of two CCs positioned at angles of 0° and 45° . Locating the two CCs is possible with the nonuniform array, whereas the uniform array does not reveal the two target positions due to the ambiguity at negative angles.

smaller target can hardly be identified from the angular power distribution using the uniform array due to the power leakage into the region of negative angles. The nonuniform array does not suffer from this drawback and allows to identify the second target at the correct angular position.

c) Achievable Accuracy Using a CC as Target: As another example, Fig. 15 shows the measurement results in polar coordinates for different positions of the CC that was moved along a straight line to investigate the achievable system accuracy. At each position, 500 measurements have been taken. The resulting worst case measurement standard deviation in range direction is 0.1 mm, the standard deviation in angle direction is 0.05° .

d) Measurements Using a Single Coin as Target: To test the system's behavior in situations with very small targets, a 50-cent Euro coin with a diameter of 24.25 mm and a thickness of 2.38 mm was used as a target. Simulations carried out using a physical optics approach result in an RCS of -8.9 dBm. The coin was placed on a wooden stick at a distance of 1.7 m

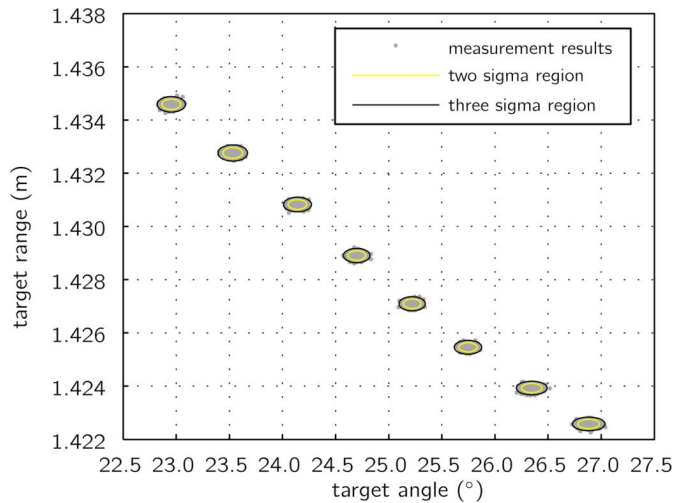


Fig. 15. Measurement results in polar coordinates of a CC moved along a straight line.

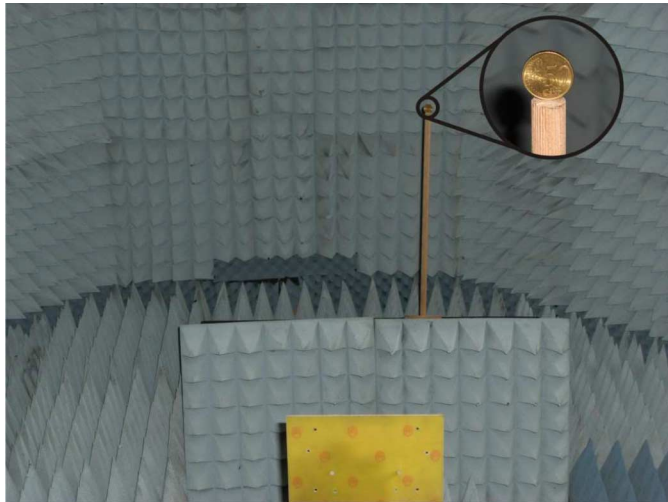


Fig. 16. Measurement setup using a 50-cent Euro coin as target. The used coin has a diameter of 24.25 mm and was placed at a distance of 1.7 m to the radar.

to the radar, as shown in Fig. 16. The resulting power distribution calculated using (30) normalized to the peak value is shown in Fig. 17. It is clearly visible that the maximum of the calculated power distribution occurs at the position of the coin. At the distance of 1.7 m, some power is spread over the entire angular range due to the constant sidelobe behavior of the designed array. Between a range from 2 to 3 m, some additional reflections are visible. They are caused by the corners in the anechoic chamber, which are also present in all other measurements. Those unwanted reflections are fortunately limited to the mentioned range interval so their influence on targets placed below a range of 2 m can be neglected.

e) Multitarget Scenario Using Three Metal Poles as Targets: To validate the system’s performance in multitarget scenarios, an example with three metal poles was used as a test case. The poles have a length of 1 m and a diameter of 25 mm. They have been placed approximately along a straight line on the x - y positions: $(-1.2\text{ m}, 0.2\text{ m})$, $(-0.5\text{ m}, 0.9\text{ m})$, and $(0.3\text{ m}, 1.7\text{ m})$. Note that the third pole is positioned at

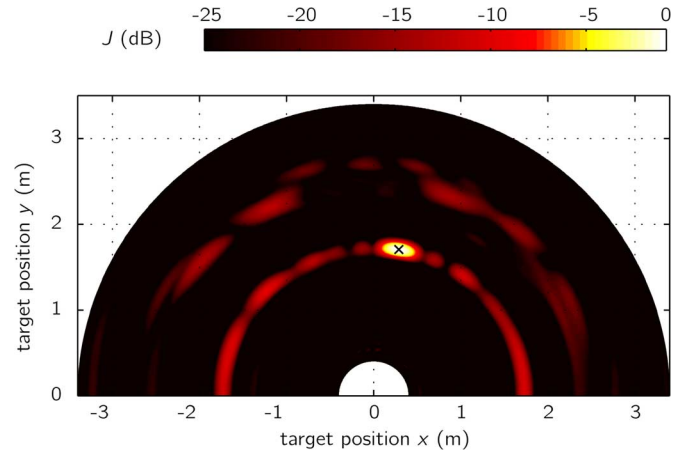


Fig. 17. Resulting power distribution using a single coin as target. The plot is normalized to the peak value (marked with a cross). The maximum of the power distribution occurs at the position of the coin.

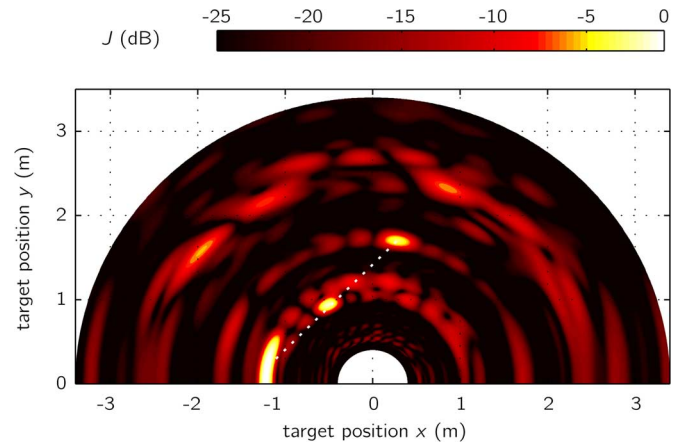


Fig. 18. Resulting power distribution using three metal poles as targets. The peaks of the power distribution are correctly located along a straight line. Reflections from the corners of the anechoic chamber are more dominant in this example since the RCSs of the poles are very small.

the location of the coin from the previous example. In Fig. 18, the calculated power distribution is depicted. It can be seen that the power maxima are located at the positions of the poles and along the straight line. This example also proves the system’s large FOV since the leftmost pole is located at an angle of 81° without causing an ambiguity in the calculated power distribution. The reflections coming from the corners of the anechoic chamber are more dominant in this example since the returned power of the poles is smaller than that of the coin. This is due to the strong dependence of the poles’ RCS onto the elevation angle. According to [42, p. 89], an angular misalignment between a pole and the radar of only 0.1° already leads to a reduction of the returned power in the range of 3 dB. Therefore, due to the nonperfect alignment of the radar look direction with the maximum of the poles’ RCS, the plotted results are normalized to a lower power value compared to the coin example. Fig. 19 shows a photograph of the setup overlaid with the power distribution. The three highest values of the distribution have been marked with crosses and it can be seen that these peak locations correspond with the true positions of the poles.

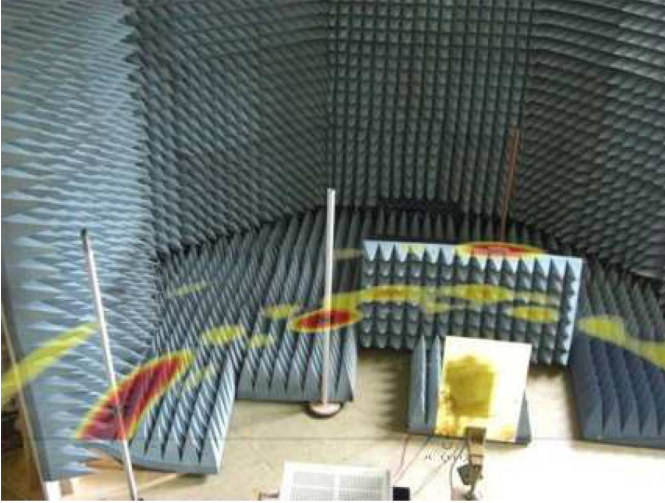


Fig. 19. Photograph of the three metal poles used as targets overlaid with the calculated power distribution shown in Fig. 18. The peaks of the power distribution (marked with crosses) correspond to the positions of the poles.



Fig. 20. Measurement setup used for moving target measurements. The photograph was taken at the beginning of the target movement and shows the case where three CCs are static, whereas one is mounted on a rail and moving.

f) Moving Target Case: To verify the applicability of the phase compensation technique introduced in Section IV-B.3, the measurement setup using a linear rail, as shown in Fig. 20, was used. First, a single moving CC was used to show the effect of the phase compensation. At each TX activation, the radar performed an upchirp and a downchirp with equal slope. The target was accelerated to 1 m/s. This velocity was reached at the middle of the rail and held constant afterwards. The resulting cost functions for this single target scenario are shown for the upchirp with and without phase compensation in Fig. 21. It can be seen from Fig. 21 that without the phase compensation, it is impossible to correctly identify the angular target position of the moving target since the estimated power is spread over the entire angular range. If the phase compensation is applied, the signals at all antennas correctly align, and thus, deliver the expected

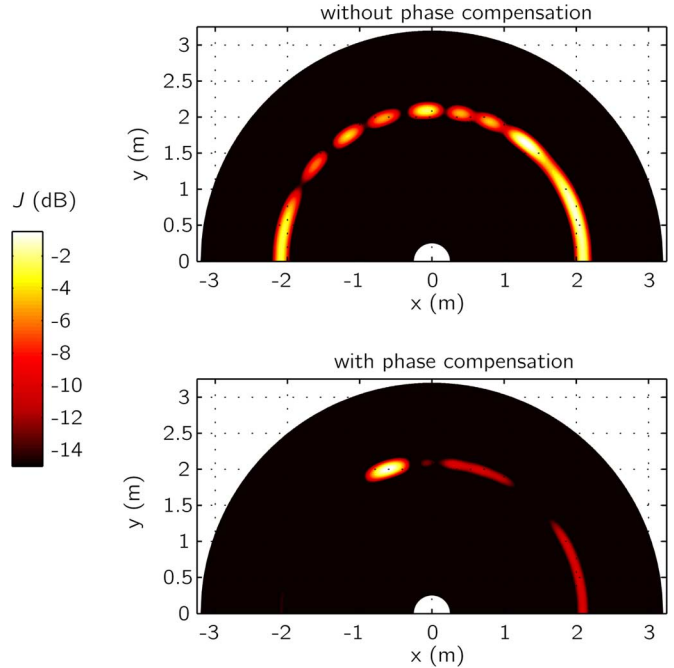


Fig. 21. Resulting cost functions for a single moving CC. The top plot shows the result from the upchirp without phase compensation, the bottom plot with phase compensation. Without phase compensation, it is impossible to estimate the targets angular position since the estimated power is spread over the whole angular range. The bottom plot shows that the phase compensation is able to correct the phase shifts due to the target movement.

result of a dominant peak at the target position shifted by the Doppler.

As a second example, a scenario with a single moving and three static targets was chosen to show that the phase compensation technique can also be applied in this case. The resulting cost functions of the target approaching the end of the rail (and thus, moving with constant velocity) are shown for both chirps in Fig. 22. All targets are visible as distinct peaks, thus the phase compensation was able to correct the phase differences between the TX activations both for moving and static targets. The target was moving away from the radar, thus for an upchirp, the calculated target range is larger than the true range. The downchirp gives a lower range with a difference between the two estimated ranges of $2\Delta r = 0.149$ m. This result corresponds well with the predicted value from (21).

2) Outdoor Scenario: The system was also used in an outdoor measurement scenario where multiple cars on a parking lot functioned as targets. For this example, the observed range was extended and for plotting purposes, a range-dependent scaling of the plotted function in decibels

$$J_{\text{plot}} = 10 \log_{10}(J_{\text{win}}) + 40 \log_{10}(r)$$

was used. This scaling is based on the assumption of point targets with an RX power corresponding to the radar equation [42, p. 9], which states that the RX power from a point like target is proportional to $1/r^4$. To emphasize the most dominant targets, only the highest 15 dB of the scaled power distribution are plotted in Fig. 23. Different dominant peaks can be observed, which can be related to multiple scattering centers from the multiple present cars. An overlay of the power distribution with a

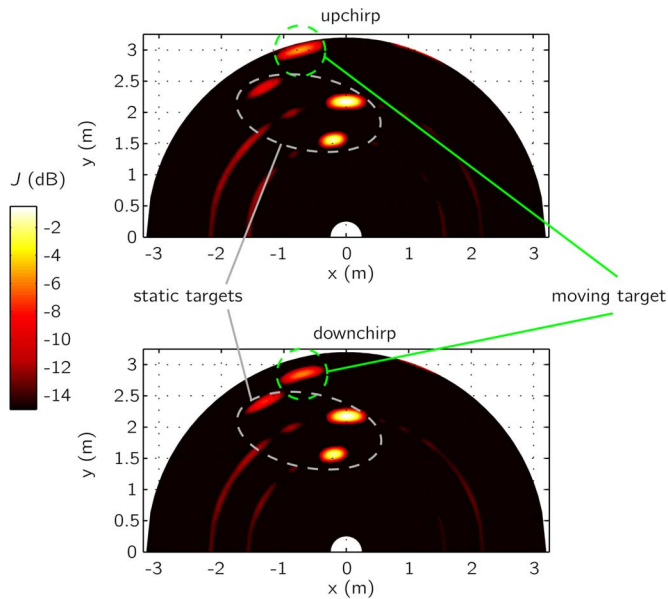


Fig. 22. Resulting cost functions for a moving target scenario. The top plot shows the result from the upchirp, the bottom plot the result from the downchirp. In both plots, the four CC are visible. The estimated static target positions are equal for upchirp and downchirp. The estimated Doppler position of the moving target shows the radial displacement due to the Doppler. The result is shown for the moving target approaching the end of the rail.

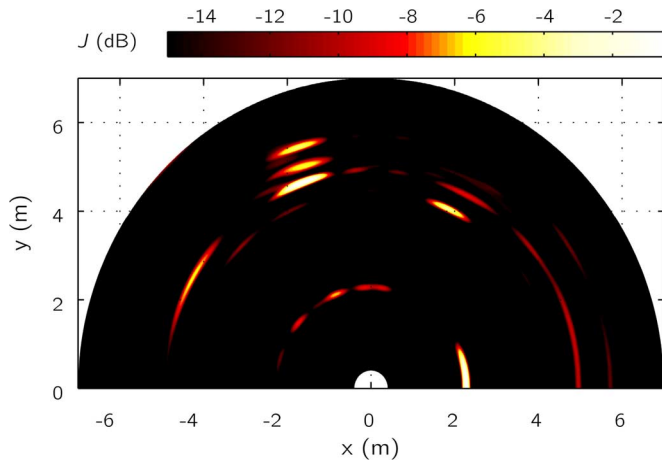


Fig. 23. Calculated power distribution of an outdoor measurement with multiple cars acting as targets. It can be seen that the scenario contains several targets located at different ranges and angles.

photograph of the measurement scenario, as shown in Fig. 24, clarifies the relation between the peaks of the power distribution and the scattering centers of the scenario. It can be clearly seen that the assumption of point-like targets is reasonable for such a scenario since parts like lamp reflectors, license plates, wheelhouses, etc. act as spatially concentrated reflectors for the electromagnetic waves.

VIII. CONCLUSION

We have presented a novel FMCW radar concept usable for 2-D target localization. The proposed system consists of a single-chip four-channel TRX with the capability to reconfigure



Fig. 24. Photograph of the measurement scenario on a parking lot with multiple cars overlaid with the calculated power distribution (cf. Fig. 23). The sundry scattering centers of the different cars can clearly be observed and related to different parts of the cars.

its channels to act only as RX or as TRX channel. This capability was used to develop a TDM-based MIMO radar. Such a technique allows to improve the angular response of the system by synthesizing virtual antennas based on the evaluation of all possible TX and RX combinations. To achieve the maximum number of different virtual antenna positions, a nonuniform array configuration was chosen. An additional advantage of using a nonuniform array is that the resulting beam patterns are unambiguous in the full angular range from -90° to 90° . The proposed concept allows the use of a delay-and-sum beamformer approach, which avoids the need for estimating the number of targets, as it is required in many superresolution algorithms. A computationally very efficient implementation based on a 2-D FFT was presented, which is another big advantage compared to more complex signal processing algorithms. To allow the application of this algorithm in moving target cases, a phase compensation technique was presented that makes use of virtual redundant antenna positions. These redundant antenna positions are always available in the presented TRX channel structure. The design of multiple arrays with different beamwidths and SLL was realized using an approach based on convex optimization. To test the proposed principle, a prototype frontend was built and used in conjunction with existing baseband hardware to obtain measurement data. To compensate imperfections of the prototype, a calibration procedure based on the phase of the FMCW baseband signal was utilized. The realized system was used in different measurement scenarios, where the results show that the proposed concept can be used for various applications even in multitarget cases with moving targets.

ACKNOWLEDGMENT

The authors would like to thank Infineon Technologies AG, Munich, Germany, for the fabrication of the presented TRX chip.

REFERENCES

- [1] A. Natarajan, A. Komijani, X. Guan, A. Babakhani, and A. Hajimiri, "A 77-GHz phased-array transceiver with on-chip antennas in silicon: Transmitter and local LO-path phase shifting," *IEEE J. Solid-State Circuits*, vol. 41, no. 12, pp. 2807–2819, Dec. 2006.
- [2] H.-P. Forstner, H. Knapp, H. Jäger, E. Kolmhofer, J. Platz, F. Starzer, M. Treml, J. Böck, K. Aufinger, R. Lachner, T. Meister, R. Schäfer, D. Lukashevich, A. Fischer, F. Reininger, L. Maurer, J. Minichhofer, and D. Steinbuch, "A 77 GHz 4-channel automotive radar transceiver in SiGe," in *Proc. IEEE Radio Freq. Integr. Circuits Symp.*, Atlanta, GA, Jun. 2008, pp. 233–236.
- [3] M.-S. Lee, V. Katkovnik, and Y.-H. Kim, "System modeling and signal processing for a switch antenna array radar," *IEEE Trans. Signal Process.*, vol. 52, no. 6, pp. 1513–1523, Jun. 2004.
- [4] H. L. v. Trees, *Detection, Estimation, and Modulation Theory, Part IV, Optimum Array Processing*. New York: Wiley, 2002.
- [5] R. Schmidt, "Multiple emitter location and signal parameter estimation," *IEEE Trans. Antennas Propag.*, vol. AP-34, no. 3, pp. 276–280, Mar. 1986.
- [6] R. Roy and T. Kailath, "Esprit-estimation of signal parameters via rotational invariance techniques," *IEEE Trans. Acoust., Speech, Signal Process.*, vol. 37, no. 7, pp. 984–995, Jul. 1989.
- [7] B. Widrow, K. Duvall, R. Gooch, and W. Newman, "Signal cancellation phenomena in adaptive antennas: Causes and cures," *IEEE Trans. Antennas Propag.*, vol. AP-30, no. 3, pp. 469–478, May 1982.
- [8] T.-J. Shan, M. Wax, and T. Kailath, "On spatial smoothing for direction-of-arrival estimation of coherent signals," *IEEE Trans. Acoust., Speech, Signal Process.*, vol. ASSP-33, no. 4, pp. 806–811, Aug. 1985.
- [9] P. Wenig, M. Schoor, O. Gunther, B. Yang, and R. Weigel, "System design of a 77 GHz automotive radar sensor with superresolution DOA estimation," in *Proc. Int. Signals, Syst., Electron. Symp.*, Montreal, QC, Canada, Jul. 2007, pp. 537–540.
- [10] P. Stoica and Y. Selen, "Model-order selection: A review of information criterion rules," *IEEE Signal Process. Mag.*, vol. 21, no. 4, pp. 36–47, Jul. 2004.
- [11] P. Chen, T. J. Wu, and J. Yang, "A comparative study of model selection criteria for the number of signals," *IET Radar Sonar Navig.*, vol. 2, no. 3, pp. 180–188, Jun. 2008.
- [12] F. C. Robey, S. Coultts, D. Weikle, J. C. McHarg, and K. Cuomo, "MIMO radar theory and experimental results," in *38th Asilomar Conf. Signals, Syst., Comput. Conf. Rec.*, Pacific Grove, CA, Nov. 2004, vol. 1, pp. 300–304.
- [13] A. Moffet, "Minimum-redundancy linear arrays," *IEEE Trans. Antennas Propag.*, vol. AP-16, no. 2, pp. 172–175, Mar. 1968.
- [14] I. Gupta and A. Ksienski, "Effect of mutual coupling on the performance of adaptive arrays," *IEEE Trans. Antennas Propag.*, vol. AP-31, no. 5, pp. 785–791, Sep. 1983.
- [15] C. C. Yeh, M. L. Leou, and D. R. Ucci, "Bearing estimations with mutual coupling present," *IEEE Trans. Antennas Propag.*, vol. 37, no. 10, pp. 1332–1335, Oct. 1989.
- [16] C. Wagner, H.-P. Forstner, G. Haider, A. Stelzer, and H. Jäger, "A 79-GHz single-chip radar transceiver with switchable TX and LO feedthrough in a silicon-germanium technology," in *Proc. IEEE Bipolar/BiCMOS Circuits Technol. Meeting*, Monterey, CA, Oct. 2008, pp. 105–108.
- [17] A. Haimovich, R. Blum, and L. Cimini, "MIMO radar with widely separated antennas," *IEEE Signal Process. Mag.*, vol. 25, no. 1, pp. 116–129, 2008.
- [18] J. Li, P. Stoica, L. Xu, and W. Roberts, "On parameter identifiability of MIMO radar," *IEEE Signal Process. Lett.*, vol. 14, no. 12, pp. 968–971, Dec. 2007.
- [19] N. Kees, E. Schmidhammer, and J. Detlefsen, "Improvement of angular resolution of a millimeterwave imaging system by transmitter location multiplexing," in *IEEE MTT-S Int. Microw. Symp. Dig.*, Orlando, FL, May 1995, vol. 2, pp. 969–972.
- [20] Y. Asano, S. Ohshima, T. Harada, M. Ogawa, and K. Nishikawa, "Proposal of millimeter-wave holographic radar with antenna switching," in *IEEE MTT-S Int. Microw. Symp. Dig.*, Phoenix, AZ, 2001, vol. 2, pp. 1111–1114.
- [21] W. Mayer, A. Gronau, W. Menzel, and H. Leier, "A compact 24 GHz sensor for beam-forming and imaging," in *Proc. 9th Int. Control, Automat., Robot., Vision Conf.*, Singapore, Dec. 2006, pp. 1–6.
- [22] M. Steinhauer, H.-O. Ruoß, H. Irion, and W. Menzel, "Millimeter-wave-radar sensor based on a transceiver array for automotive applications," *IEEE Trans. Microw. Theory Techn.*, vol. 56, no. 2, pp. 261–269, Feb. 2008.
- [23] A. G. Stove, "Linear FMCW radar techniques," *Proc. Inst. Elect. Eng.—Radar and Signal Process.*, vol. 139, no. 5, pt. F, pp. 343–350, Oct. 1992.
- [24] S. Schuster, S. Scheiblhofer, L. Reindl, and A. Stelzer, "Performance evaluation of algorithms for SAW-based temperature measurement," *IEEE Trans. Ultrason., Ferroelectr., Freq. Control*, vol. 53, no. 6, pp. 1177–1185, Jun. 2006.
- [25] R. Feger, S. Schuster, S. Scheiblhofer, and A. Stelzer, "Sparse antenna array design and combined range and angle estimation for FMCW radar sensors," in *Proc. IEEE Radar Conf.*, Rome, Italy, 2008, pp. 494–499.
- [26] E. Fishler, A. Haimovich, R. Blum, D. Chizhik, L. Cimini, and R. Valenzuela, "MIMO radar: An idea whose time has come," in *Proc. IEEE Radar Conf.*, Philadelphia, PA, Apr. 2004, pp. 71–78.
- [27] J. Li and P. Stoica, "MIMO radar with colocated antennas," *IEEE Signal Process. Mag.*, vol. 24, no. 5, pp. 106–114, Sep. 2007.
- [28] P. Stoica and R. L. Moses, *Introduction to Spectral Analysis*. Upper Saddle River, NJ: Prentice-Hall, 1997.
- [29] S. M. Kay, *Fundamentals of Statistical Signal Processing, Volume I: Estimation Theory*. Englewood Cliffs, NJ: Prentice-Hall, 1993.
- [30] C. I. Coman, I. E. Lager, and L. P. Ligthart, "Design considerations in sparse array antennas," in *Proc. 3rd Eur. Radar Conf.*, Manchester, U.K., Sep. 2006, pp. 72–75.
- [31] L. Rabiner, R. Schafer, and C. Rader, "The chirp z -transform algorithm," *IEEE Trans. Audio Electroacoust.*, vol. AE-17, no. 2, pp. 86–92, Jun. 1969.
- [32] Q. H. Liu and N. Nguyen, "An accurate algorithm for nonuniform fast Fourier transforms (NUFFT's)," *IEEE Microw. Guided Wave Lett.*, vol. 8, no. 1, pp. 18–20, Jan. 1998.
- [33] B. R. Mahafza, *Radar Systems Analysis and Design Using MATLAB*. Boca Raton, FL: CRC, 2000.
- [34] C. Dolph, "A current distribution for broadside arrays which optimizes the relationship between beam width and side-lobe level," *Proc. IRE*, vol. 34, no. 6, pp. 335–348, Jun. 1946.
- [35] H. J. Riblet, "Discussion on a current distribution for broadside arrays which optimizes the relationship between beam width and side-lobe level," *Proc. IRE*, vol. 35, no. 5, pp. 489–492, May 1947.
- [36] H. Lebrecht and S. Boyd, "Antenna array pattern synthesis via convex optimization," *IEEE Trans. Signal Process.*, vol. 45, no. 3, pp. 526–532, Mar. 1997.
- [37] M. Grant and S. Boyd, "CVX: MATLAB software for disciplined convex programming," Stanford Univ., Stanford, CA, Jun. 2008. [Online]. Available: <http://stanford.edu/~boyd/cvx>
- [38] Z. Tong, C. Wagner, R. Feger, A. Stelzer, and E. Kolmhofer, "A novel differential microstrip patch antenna and array at 79 GHz," in *Proc. Int. Antennas Propag. Symp.*, Taipei, Taiwan, 2008, pp. 276–280.
- [39] H. P. Forstner, H. Knapp, C. Gamsjäger, H. M. Rein, J. Bock, T. Meister, and K. Aufinger, "A 19 GHz VCO downconverter MMIC for 77 GHz automotive radar frontends in a SiGe bipolar production technology," in *Proc. 37th Eur. Microw. Conf.*, Munich, Germany, Oct. 2007, pp. 1457–1460.
- [40] C. Wagner, A. Stelzer, and H. Jäger, "PLL architecture for 77-GHz FMCW radar systems with highly-linear ultra-wideband frequency sweeps," in *IEEE MTT-S Int. Microw. Symp. Dig.*, San Francisco, CA, Jun. 2006, pp. 399–402.
- [41] A. Haderer, C. Wagner, R. Feger, and A. Stelzer, "A 77-GHz FMCW RF front-end sensor with FPGA and DSP support," in *Proc. Int. Radar Symp.*, Wrocław, Poland, May 2008, pp. 65–70.
- [42] D. K. Barton, *Radar System Analysis and Modeling*. Norwood, MA: Artech House, 2004.



Reinhard Feger (S'08) was born in Kufstein, Austria, in 1980. He received the Dipl.-Ing. (M.Sc.) degree in mechatronics from Johannes Kepler University, Linz, Austria in 2005, and is currently working toward the Ph.D. degree at the Johannes Kepler University.

In 2005, he joined the Institute for Communications and Information Engineering, Johannes Kepler University, as a Research Assistant. In 2007, he became a member of the Christian Doppler Laboratory for Integrated Radar Sensors, Johannes Kepler University. His research topics are radar signal processing, as well as radar system design for industrial and automotive radar sensors.



Christoph Wagner (S'06) was born in Zwettl, Austria, in 1980. He received the M.Sc. degree in mechatronics from the Johannes Kepler University, Linz, Austria in 2006, and is currently working toward the Ph.D. degree at the Johannes Kepler University.

In 2006, he joined Danube Integrated Circuit Engineering (DICE), Linz, Austria. In 2007, he became a member of the Christian Doppler Laboratory for Integrated Radar Sensors, Johannes Kepler University. His research interests include circuit and system design for millimeter-wave and microwave radar

sensors, with emphasis on digitally intensive techniques for RF imperfection mitigation.



Stefan Schuster (S'03–M'07) was born in Linz, Austria, in 1978. He received the Dipl.-Ing. (M.Sc.) degree in mechatronics and Dr. techn. degree (Ph.D.) in mechatronics from Johannes Kepler University, Linz, Austria, in 2003 and 2007, respectively.

He is currently with the Christian Doppler Laboratory for Integrated Radar Sensors, Institute for Communications and Information Engineering (ICIE), Johannes Kepler University. His research interests include statistical signal processing, parameter estimation, radar signal processing, as well as

RF system design.



Stefan Scheiblhofer (S'03–M'07) was born in Linz, Austria, in 1979. He received the Dipl.-Ing. (M.Sc.) degree in mechatronics and Dr. techn. (Ph.D.) degree in mechatronics from Johannes Kepler University, Linz, Austria, in 2003 and 2007, respectively.

He is currently with the Christian Doppler Laboratory for Integrated Radar Sensors, Institute for Communications and Information Engineering, Johannes Kepler University. His primary research interests concern advanced radar system concepts, development of radar signal processing algorithms,

statistical signal processing, RF design, and its application to automotive radar applications.



Herbert Jäger (S'97–M'04) was born in Linz, Austria, in 1975. He received the Dipl.-Ing. (M.Sc.) degree (with distinction) in electrical engineering (communication engineering) from the Vienna University of Technology, Austria, in 2000, the Dr. techn. (Ph.D.) degree (with distinction) from Johannes Kepler University, Linz, Austria in 2003, and the Postgraduate M.Sc. degree in engineering management (with distinction) at the Continuing Education Center, Vienna University of Technology, Vienna, Austria, in 2008.

In 2003, he performed his doctoral research with M/A-COM, Cork, Ireland. He is currently with Danube Integrated Circuits Engineering (DICE) GmbH, Linz, Austria, where he is focused on future generations of automotive millimeter-wave radar sensors and the development of suitable chipsets.

Dr. Jäger was the recipient of an achievement scholarship during his diploma studies.



Andreas Stelzer (M'00) was born in Haslach an der Mühl, Austria, in 1968. He received the Diploma Engineer degree in electrical engineering from the Technical University of Vienna, Vienna, Austria, and the Dr.techn. degree (Ph.D.) in mechatronics (with *sub auspiciis praesidentis rei publicae* honors) from the Johannes Kepler University, Linz, Austria, in 2000.

In 2003, he became an Associate Professor with the Institute for Communications and Information Engineering. Since 2003, he has been a key Researcher for the Linz Center of Competence in

Mechatronics (LCM) and currently for the 2008–founded Austrian Center of Competence in Mechatronics (ACCM), where he is responsible for numerous industrial projects. Since 2007, he has been Head of the Christian Doppler Laboratory for Integrated Radar Sensors, Johannes Kepler University. He has authored or coauthored over 180 journal and conference papers. He is a reviewer for international journals and conferences. His research is focused on microwave sensor systems for industrial and automotive applications, RF- and microwave subsystems, surface acoustic wave (SAW) sensor systems and applications, as well as digital signal processing for sensor signal evaluation.

Dr. Stelzer is a member of the Austrian ÖVE. He has served as an associate editor for the IEEE MICROWAVE AND WIRELESS COMPONENTS LETTERS. He was the recipient of several awards including the EEEfCOM Innovation Award and the European Microwave Association (EuMA) Radar Prize at the European Radar Conference. He was also the recipient of the 2008 IEEE Microwave Theory and Techniques Society (IEEE MTT-S) Outstanding Young Engineer Award.